

RESEARCH ARTICLE

Enhanced performance of a parallel manipulator with hybrid joint-space and task-space control approaches

Eyyup Sincar  and Zeki Y. Bayraktaroglu 

Mechanical Engineering Department, Istanbul Technical University, Istanbul, Turkey

Corresponding author: Eyyup Sincar; Email: sincar21@itu.edu.tr

Received: 28 June 2024; **Revised:** 30 November 2024; **Accepted:** 6 January 2025

Keywords: parallel manipulator; hybrid control; joint-space control; task-space control; combined control

Abstract

This paper introduces two enhanced control approaches to improve the performance of parallel manipulators, addressing their inherent nonlinear dynamics and complex structure. The first approach results in a hybrid control system in joint space, integrating acceleration-based control, sliding mode, and disturbance observer techniques. The control system is designed to correct tracking errors and compensate for generalized disturbances, thus improving accuracy in tracking reference positions. The second approach merges the joint-space and task-space formulations, implementing proportional-derivative controllers in task space to manage the end-effector positions while maintaining safe operational configurations. The stability of the proposed controllers is demonstrated through Lyapunov analysis, while their performance is validated through comprehensive simulations and real-time experiments.

1. Introduction

In the realm of mechatronic systems, parallel manipulators (PMs) have gained significant attention due to their inherent advantages such as high stiffness, high precision, high load-to-weight ratio, and highly responsive capabilities due to their parallel leg configuration, where the moving platform is connected to the base by multiple parallel legs. The attractive features of PMs make them well suited for a wide range of applications in various industries. A prime example of this is the Stewart platform, a 6-degree-of-freedom (DoF) mechanism comprised of two bodies connected by six extensible legs [1]. In addition to traditional applications such as automotive, testing, and simulation, PMs are utilized in various advanced fields including robotic-assisted surgery, virtual and augmented reality, arc welding, haptic operations, inspection and surveillance, wave compensation, UAV stabilization, and precision assembly as given by [2–5].

With growing interest in PMs across industry and academia, their potential has become increasingly apparent. However, realizing this potential requires overcoming several challenges related to the inherent complex kinematic structures, nonlinear dynamics, coupled actuation and redundancy, significant flexibility, backlash, and friction [6–9]. Consequently, the mathematical representation of a robot typically serves as an approximation of the actual system, leading to unavoidable modeling inaccuracies. Therefore, there is a demand for control approaches characterized by robustness, adaptability, rapid convergence, and simplicity of structure.

Due to its straightforward design and widespread adoption among engineers, PD/PID controls have found extensive use in various industrial domains, including PM robotic applications [10–12]. In order to obtain asymptotic stability, some feedforward terms are also added to PD/PID terms [13–14]. Such simple techniques may be appropriate for relatively slow systems with moderate tracking performance. To fully leverage their dynamic capabilities and achieve desired tracking accuracy, sophisticated control schemes are also proposed in the literature. Adaptive control approaches for PMs are proposed in

[15–17]. Sliding mode control (SMC) has emerged as a highly developed advanced control technique within the field of robotics. Robust variable structure controllers utilizing SMC are inherently appealing in the realm of PMs due to their ability to handle uncertainties effectively, provide excellent transient performance with minimal tracking error, and deliver rapid responses. To address the limitations associated with SMC – notably chattering and the requirement for prior knowledge of perturbation bounds – researchers have proposed several advanced methods and modifications to the traditional SMC approach [18–21]. Reinforcement learning, artificial neural networks, and fuzzy control methods have been proposed as intelligent control techniques for PMs [22–25]. In addition, various control techniques have been suggested such as model predictive control, disturbance rejection control, computed torque control, observer-based control, H-infinity control, and passivity-based control for PM [26–29]. Nevertheless, individual control methods often struggle to address the diverse complexities of PMs. In recent years, hybrid control fusion techniques have emerged as an effective solution to overcome these challenges. Some examples of hybrid control combinations include SMC with PD control, computed torque control with PD, and SMC with adaptive observer [30–32]. However, most studies have been validated solely by computer simulations.

In the realm of PMs, control strategies fall primarily into two categories: joint-space control and task-space control. Joint-space control offers a simpler approach, treating each leg of the manipulator as an independent system. This method is prevalent in industrial settings and utilizes basic controllers for individual legs. However, neglecting the dynamic interactions between legs (coupling effects) can lead to synchronization issues and low tracking performance [33]. In contrast, task-space control prioritizes superior performance by accounting for coupling between the manipulator's legs. This necessitates more complex control algorithms due to the multiple-input/multiple-output nature of the system. While offering better performance, task-space control relies on real-time position and velocity measurements, often requiring expensive sensors, limiting its practicality in certain situations [34].

This paper introduces two novel control systems for PMs. The first control system is based on a hybrid control approach within the joint space, merging acceleration-based control (AbC) with sliding mode and disturbance observer (DOB) techniques. The objective is to achieve high-precision position tracking while effectively managing external disturbances and model uncertainties. The AbC method likely focuses on the dynamic aspects of the system, using acceleration commands to drive the system toward the desired state. The SMC part enhances the robustness of the controller against uncertainties inherent in the system model, and the DOB actively compensates for external disturbances that may affect the manipulator's tracking performances.

The second control system is based on combined joint-space and task-space formulations, which simultaneously address control in both joint and task spaces. In task space, a PD controller is designed to regulate the end-effector positions. This integrated control approach aims to improve precision not only in individual joint movements but also in achieving the desired end-effector positions and orientations. In addition, the control algorithm can be designed to prioritize configurations that maintain a safe and stable operational space, minimizing the risk of encountering singularities during manipulator movements.

The paper is structured as follows. Section 2 provides an overview of the mathematical foundations of PMs. In Section 3, the design of the proposed control techniques and their stability analysis are discussed. Section 4 presents the simulation results obtained from the implementation of the proposed control techniques. This is followed by Section 5, which describes the experimental verification of the control techniques. Finally, Section 6 presents the conclusions drawn from the study.

2. Mathematical modeling

2.1. Kinematics

2.1.1. Inverse kinematics

In this study, simulation and experimentation are conducted on a 6-DoF PM. It consists of a fixed base (lower) and a moving (upper or end-effector) platform (frames) connected by six extendable legs. The legs are connected to the fixed base via spherical or universal joints and to the moving platform via

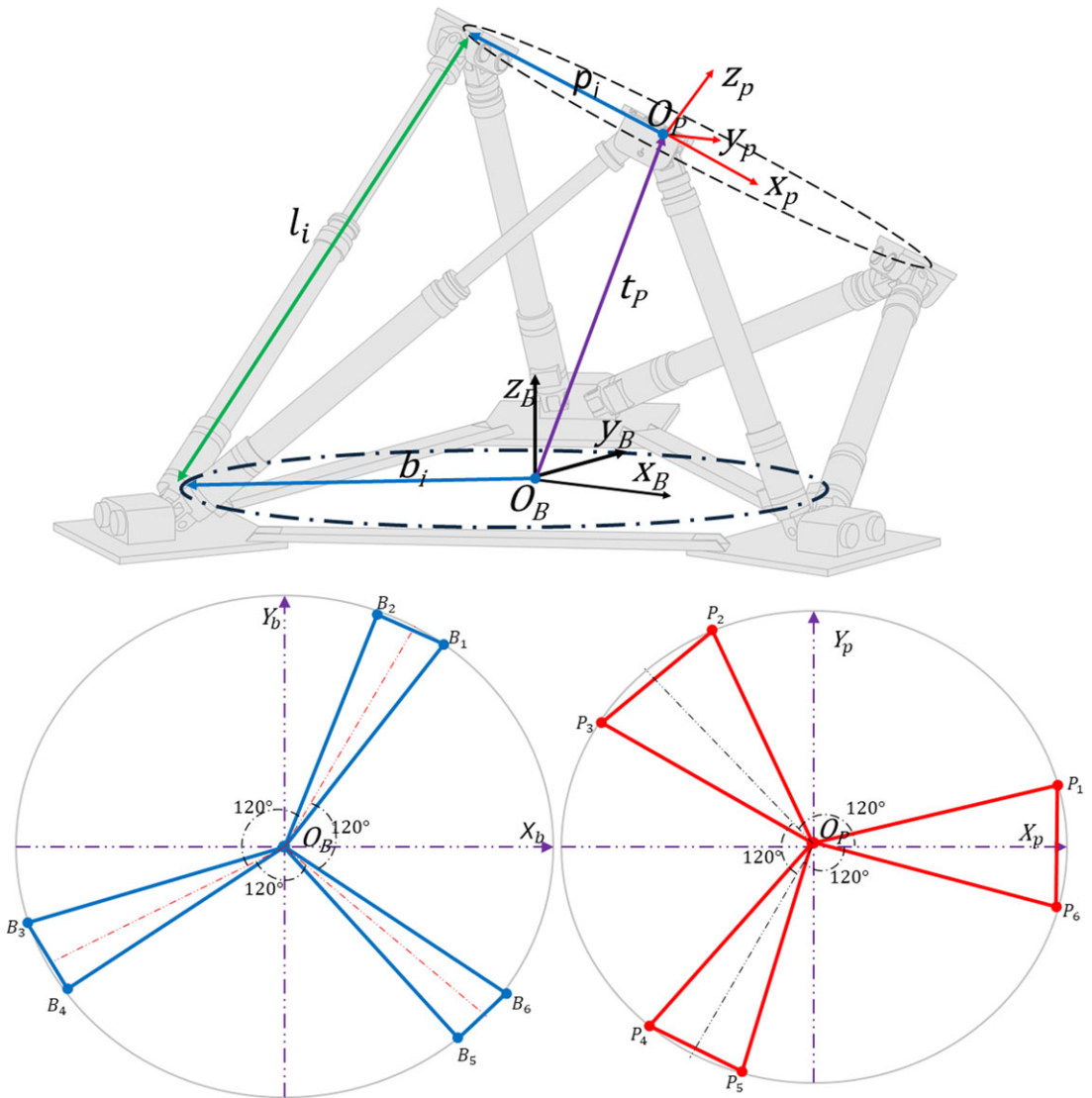


Figure 1. Kinematic configurations of the 6-DoF parallel manipulator.

universal joints. 6-DoF robot involves linear position and orientations as represented in Figure 1. Linear motions encompass movements along the longitudinal (surge), lateral (sway), and vertical (heave) axes. Angular movements, on the other hand, are described by rotations about x- (roll), y- (pitch), and z-axes (yaw), respectively. The inverse kinematics problem of PM robot focuses on determining the required leg lengths corresponding to a desired position and orientation of the moving platform, which is essential for control of moving platform and ensuring the robot’s ability to achieve complex tasks with required accuracy.

To derive the equations of inverse kinematics, we establish two reference frames, B and P , fixed to the base and moving platform, respectively, with origins O_B and O_P . The connection points of the lower and upper plate joints are designated as B_i and P_i , respectively, where $i = 1, \dots, 6$. The angles between B_1 to B_2 and B_3 to B_5 are set to 120° to symmetrically distribute connection points on the base plate, a symmetry also maintained for the upper platform. The angles between adjacent joints on the upper platform are denoted as θ_p , while those on the lower platform are denoted as θ_b as shown in Figure 1.

The position vectors of the centers of spherical joints in frame P are denoted by \mathbf{P}_i and can be expressed as follows:

$$\mathbf{P}_i = \begin{bmatrix} r_p \cos(\lambda_{P,i}) \\ r_p \sin(\lambda_{P,i}) \\ P_{iz} \end{bmatrix} = \begin{bmatrix} P_{ix} \\ P_{iy} \\ P_{iz} \end{bmatrix} \tag{1}$$

where λ_p is the upper frame joints' position angles relative to the moving frame O_p axis and r_p is the radius of the moving platform passing through the connecting points.

Similarly, the position vectors of the centers of spherical joints in frame B are denoted by \mathbf{B}_i and can be expressed as follows:

$$\mathbf{B}_i = \begin{bmatrix} r_B \cos(\lambda_{B,i}) \\ r_B \sin(\lambda_{B,i}) \\ B_{iz} \end{bmatrix} = \begin{bmatrix} B_{ix} \\ B_{iy} \\ B_{iz} \end{bmatrix} \tag{2}$$

where λ_B is the lower frame joints' position angles relative to the fixed frame O_B axis and r_B is the radius of the fixed platform passing through the connecting points.

The 6-DoF of the upper frame including three translations and three rotations are defined within the following vector:

$$\mathbf{X} = [x \quad y \quad z \quad \alpha \quad \beta \quad \gamma]^T \tag{3}$$

In this context, x , y , and z denote surge, sway, and heave translations, respectively, and α , β , and γ represent roll, pitch, and yaw rotations of the moving platform relative to the fixed frame O_B . The inverse kinematics of a PM typically provide a unique solution. Specifically, when the position and orientation of the upper platform are specified, the lengths of the legs corresponding to these configurations can be precisely determined using the inverse kinematics model. This method employs closed-loop vectors based on geometric relationships and trigonometry within the system. Subsequently, the leg vector pointing from attachment point B_i to attachment point P_i can be expressed as follows:

$$\mathbf{l}_i^B = \mathbf{t}_p^B + \mathbf{R}_{\alpha\beta\gamma} \cdot \mathbf{p}_i^P - \mathbf{b}_i^B = \mathbf{t}_p^B + \underbrace{\mathbf{R}_z(\gamma) \cdot \mathbf{R}_y(\beta) \cdot \mathbf{R}_x(\alpha)}_{\text{Rotation Matrices}} \cdot \mathbf{p}_i^P - \mathbf{b}_i^B \tag{4}$$

where $\mathbf{t}_p^B = [p_x \ p_y \ p_z]^T$ is the moving platform translation vector, with respect to the base origin O_B , and $\mathbf{p}_i^P = [P_{ix} \ P_{iy} \ P_{iz}]^T$ and $\mathbf{b}_i^B = [B_{ix} \ B_{iy} \ B_{iz}]^T$ are the translational offset vectors of the i^{th} leg on the moving and base platforms, respectively. The matrix $\mathbf{R}_{\alpha\beta\gamma}$ representing the orientation of the frame P with respect to frame B is expressed as follows:

$$\mathbf{R}_{\alpha\beta\gamma} = [\mathbf{R}_z(\gamma) \cdot \mathbf{R}_y(\beta) \cdot \mathbf{R}_x(\alpha)] = \begin{bmatrix} c\alpha c\beta & -s\alpha c\gamma + c\alpha s\beta s\gamma & s\alpha s\gamma + c\alpha s\beta c\gamma \\ s\alpha c\beta & c\alpha c\gamma + s\alpha s\beta s\gamma & -c\alpha s\gamma + s\alpha s\beta c\gamma \\ -s\beta & c\beta s\gamma & c\beta c\gamma \end{bmatrix} = \begin{bmatrix} r_{11} & r_{12} & r_{13} \\ r_{21} & r_{22} & r_{23} \\ r_{31} & r_{32} & r_{33} \end{bmatrix} \tag{5}$$

where c and s denote, respectively $\cos(\cdot)$ and $\sin(\cdot)$. From Eq. (4), the length of the i^{th} leg can be calculated by $\|\mathbf{l}_i\|$, which solves the six leg lengths of the PM robot. Hence the complete solution for the inverse kinematics can be expressed as follows:

$$\|\mathbf{l}_i\| = \sqrt{[(\mathbf{t}_p^B + \mathbf{R}_{\alpha\beta\gamma} \cdot \mathbf{p}_i^P - \mathbf{b}_i^B)^T (\mathbf{t}_p^B + \mathbf{R}_{\alpha\beta\gamma} \cdot \mathbf{p}_i^P - \mathbf{b}_i^B)]} \tag{6}$$

for $i = 1, 2, \dots, 6$

2.1.2. Kinematic Jacobian

For parallel robots, the direct kinematic problem (finding the end-effector position given the joint positions) is often difficult to solve due to their closed-loop structure. Therefore, the inverse kinematic

problem (finding the joint positions given the end-effector position) is typically solved first. Once the inverse kinematics are known, the inverse kinematic Jacobian can be derived. It's used to connect joint velocities and forces to the end-effector velocities, torque, and forces. Moreover, the characteristics of the Jacobian are frequently employed in examining kinematic singularities. The leg positions being functions of end-effector positions are defined as follows:

$$l_i = f_i(x, y, z, \alpha, \beta, \gamma) = f_i(\mathbf{X}) \quad \text{for } i = 1, 2, \dots, 6 \tag{7}$$

The leg velocities, in terms of the upper platform velocities, are obtained by applying the chain rule to the partial derivatives of the functions f_i . This results in the derivatives of l_i being expressed as functions of the derivatives of $x, y, z, \alpha, \beta, \gamma$.

$$\delta l_i = \frac{\partial f_i}{\partial x} \delta x + \frac{\partial f_i}{\partial y} \delta y + \frac{\partial f_i}{\partial z} \delta z + \frac{\partial f_i}{\partial \alpha} \delta \alpha + \frac{\partial f_i}{\partial \beta} \delta \beta + \frac{\partial f_i}{\partial \gamma} \delta \gamma \tag{8}$$

Dividing both sides by the differential time element δt and arranging in matrix form yields:

$$\begin{bmatrix} \dot{l}_1 \\ \dot{l}_2 \\ \vdots \\ \dot{l}_6 \end{bmatrix} = \begin{bmatrix} \frac{\partial f_1}{\partial x} & \frac{\partial f_1}{\partial y} & \frac{\partial f_1}{\partial z} & \frac{\partial f_1}{\partial \alpha} & \frac{\partial f_1}{\partial \beta} & \frac{\partial f_1}{\partial \gamma} \\ \frac{\partial f_2}{\partial x} & \frac{\partial f_2}{\partial y} & \frac{\partial f_2}{\partial z} & \frac{\partial f_2}{\partial \alpha} & \frac{\partial f_2}{\partial \beta} & \frac{\partial f_2}{\partial \gamma} \\ \vdots & \vdots & \vdots & \vdots & \vdots & \vdots \\ \frac{\partial f_6}{\partial x} & \frac{\partial f_6}{\partial y} & \frac{\partial f_6}{\partial z} & \frac{\partial f_6}{\partial \alpha} & \frac{\partial f_6}{\partial \beta} & \frac{\partial f_6}{\partial \gamma} \end{bmatrix} \begin{bmatrix} \dot{x} \\ \dot{y} \\ \dot{z} \\ \dot{\alpha} \\ \dot{\beta} \\ \dot{\gamma} \end{bmatrix} \tag{9}$$

Let $J^{-1} \in \mathbb{R}^{6 \times 6}$ denote the inverse Jacobian (kinematic Jacobian) matrix composed of these partial derivatives. The forward and inverse kinematics are then expressed as follows:

$$\dot{\mathbf{X}} = \mathbf{J} \dot{\mathbf{i}} \tag{10}$$

$$\dot{\mathbf{i}} = J^{-1} \dot{\mathbf{X}} \tag{11}$$

Here, $\mathbf{X} \in \mathbb{R}^6$ represents the task-space end-effector positions, while $\dot{\mathbf{X}}$ and $\ddot{\mathbf{X}}$ are the corresponding velocities and accelerations. $J \in \mathbb{R}^{6 \times 6}$ is the Jacobian matrix.

2.1.3. Forward kinematics

The forward kinematics determines the position and orientation of the upper platform based on the provided leg lengths. The forward kinematics of a PM involve a set of complex nonlinear differential equations, making them challenging to solve. As a result, iterative solvers such as the Newton–Raphson method are commonly used to obtain approximate solutions. The general form of the function used for forward kinematics can be given as follows:

$$\begin{aligned} F_i(x, y, z, \alpha, \beta, \gamma) = & x^2 + y^2 + (z + z_0)^2 + r_p^2 + r_b^2 \\ & + 2(r_{11}P_{ix} + r_{12}P_{iy})(p_x - B_{ix}) \\ & + 2(r_{21}P_{ix} + r_{22}P_{iy})(p_y - B_{iy}) \\ & + 2(r_{31}P_{ix} + r_{32}P_{iy})(p_z) \\ & - 2(P_x B_{ix} + P_y B_{iy}) - ||l_i||^2 \quad \text{for } i = 1, 2, \dots, 6 \end{aligned} \tag{12}$$

2.2. Dynamics

The dynamic modeling of PMs presents significant complexity and nonlinearity due to the constraints within their closed-loop structure. Multiple kinematic chains connect the moving platform to the fixed

base, causing the motion of a single joint to directly influence several others, resulting in a high degree of coupling. These closed loops also impose nonlinear geometric constraints on the system’s motion. To manage this complexity, the dynamic model is typically expressed in a general and compact form. The dynamics of the robot manipulator, considering uncertainties and disturbances, are described as follows:

$$M(\mathbf{q})\ddot{\mathbf{q}} + V(\mathbf{q}, \dot{\mathbf{q}})\dot{\mathbf{q}} + G(\mathbf{q}) + F(\dot{\mathbf{q}}) = \boldsymbol{\tau}(t) - \mathbf{d}(t) \tag{13}$$

where $\mathbf{q}(t) := [q_1(t), q_2(t), \dots, q_n(t)]^T \in \mathbb{R}^n$ denotes the joint positions, $\dot{\mathbf{q}}(t) \in \mathbb{R}^n$ the joint velocities, and $\ddot{\mathbf{q}}(t) \in \mathbb{R}^n$ the joint accelerations. $M(\mathbf{q}) \in \mathbb{R}^{n \times n}$, $V(\mathbf{q}, \dot{\mathbf{q}}) \in \mathbb{R}^{n \times n}$, $G(\mathbf{q}) \in \mathbb{R}^n$, and $F(\dot{\mathbf{q}}) \in \mathbb{R}^n$ are the inertia matrix, centripetal-Coriolis matrix, gravitational torque, and friction torque, respectively. $\mathbf{d}(t) \in \mathbb{R}^n$ and $\boldsymbol{\tau}(t) \in \mathbb{R}^n$ denote the external disturbances and input force, respectively.

Based on [10], the dynamic model satisfies the following properties:

Property 1. The inertia matrix $M(\mathbf{q})$ is symmetric positive definite and satisfies $M(\mathbf{q}) = M^T(\mathbf{q}) > 0$, where $m_1 \|x\|^2 \leq x^T M(q)x \leq m_2 \|x\|^2$ for all $x \in \mathbb{R}^n$.

Property 2. $\dot{M}(\mathbf{q})$ is bounded.

Property 3. $\dot{M}(\mathbf{q})$ is skew-symmetric and satisfies $x^T(\dot{M}(\mathbf{q}) - 2V(\mathbf{q}, \dot{\mathbf{q}}))x = 0$ for all $x \in \mathbb{R}^n$.

Property 4. The friction torque $F(\dot{\mathbf{q}})$ is uncoupled among joints and expressed as $F(\dot{\mathbf{q}}) = [f_1(\dot{q}_1), f_2(\dot{q}_2), \dots, f_n(\dot{q}_n)]^T$, where $f_i(\dot{q}_i)$ is bounded and continuous.

Property 5. The trajectory of joints positions, velocities, and accelerations $\mathbf{q}(t)$, $\dot{\mathbf{q}}(t)$, and $\ddot{\mathbf{q}}(t)$ exist and are bounded.

The system is subject to uncertainties stemming from factors such as inertia loading, unmodeled dynamics, and friction from the actuators and transmissions. These uncertainties are expected to be bounded and can be represented in the dynamic model as follows:

$$(M_n(\mathbf{q}) + \Delta M(\mathbf{q}))\ddot{\mathbf{q}} + (C(\mathbf{q}, \dot{\mathbf{q}}) + \Delta C(\mathbf{q}, \dot{\mathbf{q}}))\dot{\mathbf{q}} + G(\mathbf{q}) + \Delta G(\mathbf{q}) + F(\dot{\mathbf{q}}) = \boldsymbol{\tau}(t) - \mathbf{d}(t) \tag{14}$$

where Δ represents deviations from the nominal parameters.

The dynamic model can be rewritten in the following compact form:

$$M_n(\mathbf{q})\ddot{\mathbf{q}} + V_n(\mathbf{q}, \dot{\mathbf{q}})\dot{\mathbf{q}} + G_n(\mathbf{q}) = \boldsymbol{\tau}(t) - \boldsymbol{\tau}_{\text{dis}}(t, \mathbf{q}) \tag{15}$$

where $\boldsymbol{\tau}_{\text{dis}}(t, \mathbf{q})$ is the lumped disturbance vector defined as follows:

$$\boldsymbol{\tau}_{\text{dis}}(t, \mathbf{q}) = -\Delta M\ddot{\mathbf{q}} - \Delta V\dot{\mathbf{q}} - \Delta G - F(\dot{\mathbf{q}}) - \mathbf{d}(t) \tag{16}$$

ΔM , ΔV , and ΔG represent the corresponding modeling errors and are assumed to be bounded. The terms M_n , V_n and G_n represent the nominal dynamic model components.

3. Control system design

3.1. Hybrid control in joint space

3.1.1. Description of the controller

AbC or acceleration control (ACC) is a control strategy that directly employs joint accelerations to command robotic manipulators. By utilizing feedforward acceleration reference, AbC can potentially achieve faster behavior and more accurate tracking performance compared to traditional control methods. However, disturbances such as external forces, friction, or modeling errors can affect the system’s performance. To mitigate the effects of disturbances, a DOB is integrated into the AbC architecture as described in ref. [40]. While the AbC with DOB offers improved tracking performance and disturbance rejection, it may still struggle with highly nonlinear systems and random disturbances. In this study, a sliding mode controller is introduced alongside the AbC with DOB, constituting a hybrid controller. This hybridization allows the system to leverage the strengths of each individual method while compensating

for their respective weaknesses. Let us define the joint position errors $\mathbf{e} \in \mathbb{R}^6$ of the joints as follows:

$$\mathbf{e}(t) = \mathbf{q}_r(t) - \mathbf{q}(t) \tag{17}$$

where $\mathbf{q}_r \in \mathbb{R}^6$ is the vector of reference actuators (joints) trajectories. Let us define the sliding surface as follows:

$$\mathbf{s}(t) = \dot{\mathbf{q}}_r(t) - \dot{\mathbf{q}}(t) + \lambda(\mathbf{q}_r(t) - \mathbf{q}(t)) = \dot{\mathbf{e}}(t) + \lambda\mathbf{e}(t) \tag{18}$$

where $\mathbf{s}(t) \in \mathbb{R}^6$ represents the sliding surface, $\dot{\mathbf{e}}(t) \in \mathbb{R}^6$ is the joint tracking rate error, and $\dot{\mathbf{q}}_r(t) \in \mathbb{R}^6$ is the vector of desired velocities. $\lambda = \text{diag}(\lambda)$ with $\lambda > 0$ for $(i = 1, \dots, 6)$ is the diagonal positive definite constant matrix that determines the slope of the sliding surface.

The time derivative of the sliding surface is then given as follows:

$$\dot{\mathbf{s}}(t) = \ddot{\mathbf{q}}_r(t) - \ddot{\mathbf{q}}(t) + \lambda(\dot{\mathbf{q}}_r(t) - \dot{\mathbf{q}}(t)) = \ddot{\mathbf{e}}(t) + \lambda\dot{\mathbf{e}}(t) \tag{19}$$

Based on Eq. (15), the expression of the acceleration vector is written as follows:

$$\ddot{\mathbf{q}}(t) = M_n^{-1}(\mathbf{q})(\tau(t) - \tau_{\text{dis}}(t, \mathbf{q}) - V_n(\mathbf{q}, \dot{\mathbf{q}})\dot{\mathbf{q}} - G_n(\mathbf{q})) \tag{20}$$

Inserting Eq. (19) into Eq. (18), one gets

$$\dot{\mathbf{s}}(t) = \ddot{\mathbf{q}}_r(t) - M_n^{-1}(\mathbf{q})(\tau(t) - \tau_{\text{dis}}(t, \mathbf{q}) - V_n(\mathbf{q}, \dot{\mathbf{q}})\dot{\mathbf{q}} - G_n(\mathbf{q})) + \lambda\dot{\mathbf{e}}(t) \tag{21}$$

The system dynamics are designed to reach the sliding surface in a finite time. A common reaching law could be as follows:

$$\dot{\mathbf{s}}(t) = -k_0 \text{sgn}(\mathbf{s}(t)) - \eta\mathbf{s}(t) \tag{22}$$

where k_0 and η are positive constants and $\text{sgn}(\mathbf{s}(t))$ denotes the signum function. Based on Eq. (21) and Eq. (22), the input force or control law can be obtained as follows:

$$\tau(t) = M_n(\mathbf{q})(\ddot{\mathbf{q}}_r(t) + k_0 \text{sgn}(\mathbf{s}(t)) + \eta\mathbf{s}(t) + \lambda\dot{\mathbf{e}}(t)) + \tau_{\text{dis}}(t, \mathbf{q}) + V_n(\mathbf{q}, \dot{\mathbf{q}})\dot{\mathbf{q}} + G_n(\mathbf{q}) \tag{23}$$

Here $\tau(t)$ is control law, but $\tau_{\text{dis}}(t, q)$ contains modeling mismatch, friction, and other disturbances. In order to address these generalized disturbances, an appropriate estimation law $\tau_{\text{dob}}(t, q)$, which is the estimated output of $\tau_{\text{dis}}(t, q)$, will be incorporated into the control law. Based on [40–42], the estimation of the disturbance vector can be derived in terms of an auxiliary variable and the states of the system by utilizing the known nonlinear dynamic model of PMs as follows:

$$\tau_{\text{dob}}(t, q) = \mathbf{z} - L\dot{\mathbf{q}} \tag{24}$$

where $\tau_{\text{dob}}(t, q)$ represents the estimation of $\tau_{\text{dis}}(t, q)$, $L \in \mathbb{R}$ represents the observer gain of DOB to be tuned, and $\mathbf{z} \in \mathbb{R}$ represents the auxiliary variable vector, which can be obtained by integrating the following equation:

$$\dot{\mathbf{z}} = LM_n^{-1}(\mathbf{q})(\tau(t) - \tau_{\text{dob}}(t, \mathbf{q})) - LM_n^{-1}(\mathbf{q})(V_n(\mathbf{q}, \dot{\mathbf{q}})\dot{\mathbf{q}} - G_n(\mathbf{q})) \tag{25}$$

The dynamic equation of disturbance estimation can be obtained by taking the derivative of Eq. (24) and inserting it into Eq. (25) and Eq. (15) as follows:

$$\begin{aligned} \dot{\tau}(t, \mathbf{q})_{\text{dob}} &= LM_n^{-1}(\mathbf{q})(\tau(t) - \tau_{\text{dob}}(t, \mathbf{q}) - V_n(\mathbf{q}, \dot{\mathbf{q}})\dot{\mathbf{q}} - G_n(\mathbf{q})) \\ &\quad - LM_n^{-1}(\mathbf{q})(\tau(t) - \tau_{\text{dis}}(t, \mathbf{q}) - V_n(\mathbf{q}, \dot{\mathbf{q}})\dot{\mathbf{q}} - G_n(\mathbf{q})) \\ \dot{\tau}(t, \mathbf{q})_{\text{dob}} &= LM_n^{-1}(\mathbf{q})(\tau_{\text{dis}}(t, \mathbf{q}) - \tau_{\text{dob}}(t, \mathbf{q})) \end{aligned} \tag{26}$$

If $\dot{\tau}_{\text{dob}}$ is subtracted from both side, then Eq. (27) can be formed as follows:

$$\dot{\mathbf{e}}(t)_{\text{dis}} + LM_n^{-1}(\mathbf{q})\mathbf{e}_{\text{dis}} = \dot{\tau}(t, \mathbf{q})_{\text{dis}} \tag{27}$$

where $\mathbf{e}_{\text{dis}} = \tau_{\text{dob}}(t, \mathbf{q}) - \tau_{\text{dis}}(t, \mathbf{q}) \in \mathbb{R}^6$.

Assumption 1. *The lumped disturbance $\tau_{\text{dis}}(t, \mathbf{q})$ is bounded by $\|\tau_{\text{dis}}\|_{r>0} \leq \delta_1$, where $\delta_1 \in \mathbb{R}^+$ is a constant.*

Assumption 2. The change rate of the lump disturbance $\dot{\boldsymbol{\tau}}_{dis}(t, \mathbf{q})$ is bounded by $\|\dot{\boldsymbol{\tau}}_{dis}(t, \mathbf{q})\|_{t>0} \leq \delta_2$, where $\delta_2 \in \mathbb{R}^+$ is a constant.

With Assumptions 1–2 and L strictly positive definite, then it can be shown that the error of disturbance estimation is uniformly ultimately bounded, that is,

$$\|e_{dis}(t)\| \leq \exp(-\lambda_u(t - t_0))\|e_{dis}(t_0)\| + \frac{\delta_2}{\lambda_u} \tag{28}$$

where $\lambda_u = LM_n^{-1}(q) > 0$.

Equation (28) shows that the convergence rate and the accuracy of disturbance estimation are directly adjusted by tuning the nominal inertia matrix and the gain of the DOB.

Replacing the designed DOB $\boldsymbol{\tau}_{dob}(t, \mathbf{q})$ with $\boldsymbol{\tau}_{dis}(t, \mathbf{q})$ in Eq. (23), the control rule becomes as follows:

$$\boldsymbol{\tau}(t) = M_n(\mathbf{q}) (\ddot{\mathbf{q}}_r(t) + k_0 \operatorname{sgn}(\mathbf{s}(t)) + \eta \mathbf{s}(t) + \lambda \dot{\mathbf{e}}(t)) + \boldsymbol{\tau}_{dob}(t, \mathbf{q}) + V_n(\mathbf{q}, \dot{\mathbf{q}})\dot{\mathbf{q}} + G_n(\mathbf{q}) \tag{29}$$

where the term $\ddot{\mathbf{q}}_r(t) + \eta \mathbf{s}(t) + \lambda \dot{\mathbf{e}}(t)$ is called the reference feedforward acceleration, and it can be represented as follows:

$$\ddot{\mathbf{q}}_d(t) = \ddot{\mathbf{q}}_r(t)(\eta + \lambda)(\dot{\mathbf{e}}(t) + (\eta\lambda)\mathbf{e}(t)) = \ddot{\mathbf{q}}_r(t) + k_v \dot{\mathbf{e}}(t) + k_p \mathbf{e}(t) \tag{30}$$

where k_v and $k_p \in \mathbb{R}^{6 \times 6}$ are the diagonal velocity and position control gain matrices. Then the controller rule can be obtained as follows:

$$\mathbf{u}(t) = M_n(\mathbf{q}) (\ddot{\mathbf{q}}_d(t) + k_0 \operatorname{sgn}(\mathbf{s}(t))) + \boldsymbol{\tau}_{dob}(t, \mathbf{q}) + V_n(\mathbf{q}, \dot{\mathbf{q}})\dot{\mathbf{q}} + G_n(\mathbf{q}) \tag{31}$$

As can be seen, it is actually a form of acceleration feedforward control with integration of sliding reaching term and DOB. Hence, it represents a hybrid control approach. The controller parameters k_v and k_p are tuned by considering the nominal system dynamics only, since the model mismatch and disturbances can be compensated by sliding face and DOB.

3.1.2. Stability analysis

In order to prove the stability of the proposed controller, let us refer to the following stability theorem:

Stability Theorem: When dealing with a nonlinear uncertain dynamical system as defined by Eq. (15), the application of the robust control law outlined by Eq. (29) ensures asymptotic robust stability of the closed-loop system in the presence of model uncertainties and disturbances.

Proof: Let us consider the following Lyapunov function candidate and its time derivative:

$$V = \frac{1}{2} \mathbf{s}(t)^T \mathbf{s}(t) + \frac{1}{2} \mathbf{e}_{dis}^T \mathbf{e}_{dis} \tag{32}$$

$$\dot{V} = \mathbf{s}\dot{\mathbf{s}} + \mathbf{e}_{dis}\dot{\mathbf{e}}_{dis} \tag{33}$$

Inserting control law of Eq. (29) into Eq. (18), one gets sliding face as follows:

$$\dot{\mathbf{s}}(t) = -k_0 \operatorname{sgn} \mathbf{s}(t) - \eta \mathbf{s}(t) - M_n^{-1} \mathbf{e}_{dis} \tag{34}$$

Using Eq. (30) of DOB error dynamic with Assumption 2 of the change rate of the lump disturbance $\dot{\boldsymbol{\tau}}_{dis}(t, \mathbf{q})$ is bounded by $\|\dot{\boldsymbol{\tau}}_{dis}(t, \mathbf{q})\| \leq \delta_2$, and taking $\delta_2 = 0$, and inserting into Eq. (34) into Eq. (33), Eq. (33) yields as follows:

$$\dot{V} = \mathbf{s}(t)(-k_0 \operatorname{sgn} \mathbf{s}(t) - \eta \mathbf{s}(t) - M_n^{-1} \mathbf{e}_{dis}) - LM_n^{-1} \|\mathbf{e}_{dis}\|^2 \tag{35}$$

Expanding Eq. (35)

$$\dot{V} = -k_0 \|\mathbf{s}(t)\| - \eta \|\mathbf{s}(t)\|^2 - M_n^{-1} \mathbf{s}(t) \mathbf{e}_{dis} - LM_n^{-1} \|\mathbf{e}_{dis}\|^2 \tag{36}$$

where $k_0 \geq M_n^{-1} \|\mathbf{e}_{dis}\|_{max}$.

Consider $\|\mathbf{e}_{\text{dis}}(0)\| = \|\mathbf{e}_{\text{dis}}\|_{\text{max}}$, we have $k_0 \geq M_n^{-1}\|\mathbf{e}_{\text{dis}}(0)\|$, then

$$\dot{V} \leq -\eta\|\mathbf{s}(t)\|^2 - LM_n^{-1}\|\mathbf{e}_{\text{dis}}\|^2 \leq -k_1 \left(\frac{1}{2}\mathbf{s}(t)^T\mathbf{s}(t) + \frac{1}{2}\mathbf{e}_{\text{dis}}^T\mathbf{e}_{\text{dis}} \right) = -k_1 V \tag{37}$$

where $k_1 = 2 \min\{\eta, LM_n^{-1}\}$.

The following lemma can be used to the solution of the inequality of Eq. (37):

Lemma.[36]–[37]

Let $f, V: [0, \infty) \in \mathbb{R}$, then $\dot{V} \leq -\alpha V + f$ for $\forall t \geq t_0 \geq 0$ implies that

$$V(t) \leq e^{2\alpha(t-t_0)}V(t_0) + \int_{t_0}^t e^{2\alpha(t-\tau)}f(\tau)d\tau \tag{38}$$

for any finite constant α .

According to [39], we have the proof as follows:

Let $\omega(t) \triangleq \dot{V} - \alpha V - f$, we have $\omega(t) \leq 0$, and

$$\dot{V} = -\alpha V + f + \omega \tag{39}$$

implies that

$$V(t) = e^{-\alpha(t-t_0)}V(t_0) + \int_{t_0}^t e^{-\alpha(t-\tau)}f(\tau)d\tau + \int_{t_0}^t e^{-\alpha(t-\tau)}\omega(\tau)d\tau \tag{40}$$

Since $\omega(t) < 0$ and $\forall t \geq t_0 \geq 0$, one has the following inequality:

$$V(t) \leq e^{-\alpha(t-t_0)}V(t_0) + \int_{t_0}^t e^{-\alpha(t-\tau)}f(\tau)d\tau. \tag{41}$$

Moreover, setting $f = 0$, one has $\dot{V} \leq -\alpha V$, implying the following inequality:

$$V(t) \leq e^{-\alpha(t-t_0)}V(t_0) \tag{42}$$

If α has a positive constant value, then $V(t)$ will tend to zero exponentially.

Using above the lemma, Eq. (37) can be obtained as follows:

$$\dot{V} \leq -k_1 V \tag{43}$$

$$V(t) \leq e^{-k_1(t-t_0)}V(t_0) \tag{44}$$

Notice that the right side of inequality decreases linearly as time t increases, and so the function will converge to zero exponentially, showing the stability of the proposed controller.

It is worth noting that the sliding mode part of the control rule leads to oscillations in the controlled system due to the discontinuous nature of the sign function used in the control law. This oscillatory behavior, known as chattering, is also present in the proposed controller described in Eq. (29). To mitigate chattering, a saturation function can be employed, leading to a modification of the control law as follows:

$$\text{sat}(\dot{\mathbf{e}} + \lambda\mathbf{e}, \phi) = \begin{cases} \text{sign}(\dot{\mathbf{e}} + \lambda\mathbf{e}) & \text{if } |\dot{\mathbf{e}} + \lambda\mathbf{e}| \leq \phi \\ \frac{\dot{\mathbf{e}} + \lambda\mathbf{e}}{\phi} & \text{if } |\dot{\mathbf{e}} + \lambda\mathbf{e}| > \phi \end{cases} \tag{45}$$

The final tracking error e can be constrained within a specified precision ε , known as the boundary layer width as specified in ref. [20]. The tracking error e can be calculated as follows:

$$\varepsilon = \frac{\phi}{\lambda} \tag{46}$$

Equation (46) indicates that the final maximum tracking error can be regulated by appropriately selecting the boundary layer ϕ and the slope constant λ . Then, the final form of the hybrid joint-space control rule to be tuned is as follows:

$$\mathbf{u}(t) = \mathbf{M}_n(\mathbf{q}) (\ddot{\mathbf{q}}_d(t) + k_0 \text{sat}(\dot{\mathbf{e}} + \lambda \mathbf{e}, \phi)) + \boldsymbol{\tau}_{\text{dob}}(t, \mathbf{q}) \tag{47}$$

3.2. Combined control approach

Joint-space control of parallel robots is often preferred due to its simplicity. However, this method comes with significant drawbacks, as mechanical components like ball screws, spherical and prismatic joints, belt pulleys, and couplings introduce disturbance sources such as backlash and flexibility. These imperfections can lead to significant tracking errors, preventing the robot’s ability to perform precise motion control. In order to address these limitations, a dual approach that combines joint-space control and task-space control is proposed. This dual or combined strategy leverages the strengths of both control spaces: joint-space control manages the movement of individual joints, while task-space control ensures the accurate positioning and orientation of the robot’s end-effector. Integrating these two control mechanisms can significantly enhance the robot’s precision, making it adept for tasks that demand high levels of accuracy and reliability.

Based on the joint-space formulation of the robot dynamics, the equations of motion can be reestablished in task space by using the manipulator’s Jacobian matrix. The Jacobian relates the joint velocities and accelerations to the end-effector velocities and accelerations as follows:

$$\begin{aligned} \dot{\mathbf{X}} &= J\dot{\mathbf{q}} \\ \ddot{\mathbf{X}} &= J\ddot{\mathbf{q}} + \dot{J}\dot{\mathbf{q}} \end{aligned} \tag{48}$$

Furthermore, the Jacobian matrix maps the joint forces to the generalized end-effector forces. Pre-multiplying both sides of Eq. (13) by the transpose of the Jacobian matrix (J^T), the dynamics of the manipulator are expressed in terms of the task-space variables as follows:

$$J^T[M(\mathbf{q})\ddot{\mathbf{q}} + V(\mathbf{q}, \dot{\mathbf{q}})\dot{\mathbf{q}} + G(\mathbf{q}) + F(\dot{\mathbf{q}})] = J^T[\boldsymbol{\tau}(t) - \mathbf{d}(t)] \tag{49}$$

$$\Lambda(\mathbf{X})\ddot{\mathbf{X}} + \mu(\mathbf{X}, \dot{\mathbf{X}}) + \rho(\mathbf{X}) = \mathbf{f}(t) - \mathbf{D}(t) \tag{50}$$

where:

- $\Lambda(\mathbf{X}) = J^{-T}M(\mathbf{q})J^{-1}$ is the inertia matrix in task space,
- $\mu(\mathbf{X}, \dot{\mathbf{X}}) = J^{-T}[V(\mathbf{q}, \dot{\mathbf{q}}) - M(\mathbf{q})\dot{J}]\dot{\mathbf{q}}$ represents the centripetal-Coriolis terms in task space,
- $\rho(\mathbf{X}) = J^{-T}G(\mathbf{q})$ is the gravitational force vector in task space,
- $\mathbf{f}(t) = J^{-T}\boldsymbol{\tau}(t)$ is the generalized force vector in task space,
- $\mathbf{D}(t) = J^{-T}\mathbf{d}(t)$ represents the external disturbances in task space.

The end-effector position tracking error is defined as follows:

$$\mathbf{e}_x(t) = \mathbf{X}_r(t) - \mathbf{X}(t) \tag{51}$$

where $\mathbf{X}_r \in \mathbb{R}^6$ is the vector of position reference for the end-effector in task space.

Let us define the PD sliding surface as follows:

$$\mathbf{r}(t) = k\dot{\mathbf{e}}_x(t) + c\mathbf{e}_x(t) \tag{52}$$

where $r(t) \in \mathbb{R}^6$ is the sliding surface, $\dot{\mathbf{X}}_r(t) - \dot{\mathbf{X}}(t) = \dot{\mathbf{e}}_x(t) \in \mathbb{R}^n$ is the end-effector tracking rate error, in which $\dot{\mathbf{X}}_r(t) \in \mathbb{R}^n$ is the desired velocity trajectory. $k = \text{diag}(k)$ with $k > 0$ for $(i = 1, \dots, 6)$ is the diagonal positive definite constant matrix and $c = \text{diag}(c)$ with $c > 0$ for $(i = 1, \dots, 6)$ is the diagonal positive definite constant matrix that determines the slope of the sliding surface.

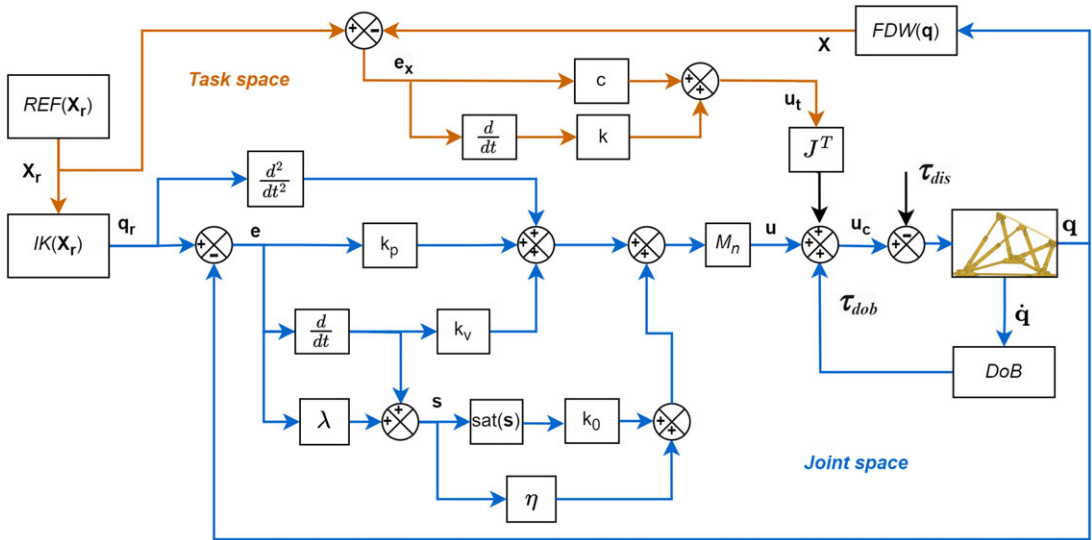


Figure 2. Block diagram of the hybrid joint-space control (in blue) and the joint-space/task-space combined control.

This controller in task space can be converted to joint space by utilizing the Jacobian matrix as follows:

$$u_t = J^T r(t) = J^T (k\dot{e}_x(t) + ce_x(t)) \tag{53}$$

where u_t is simple control rule converted from task space to joint space by Jacobian matrix.

Then, combining this task-space control rule with the derived joint-space control rule, the proposed combined control in joint and task space can be obtained as follows:

$$u_c(t) = u(t) + J^{-T}u_t(t) = M_n(q)(\ddot{q}_d(t) + k_0\text{sat}(\dot{e} + \lambda e, \phi)) + \tau_{dob}(t, q) + J^{-T}u_t(t) \tag{54}$$

where u_c is the combined control rule for both task and joint spaces. The proposed controllers' block diagram is represented in Figure 2.

One can notice that the combined control law given in Eq. (54) is an extended version of the joint-space hybrid control law proposed in Eq. (31). Parameters such as the nominal dynamic inertia M_n and the observer gain L (representing the bandwidth of the DOB), as well as the gains for velocity and position errors of the end-effector and joints, should be tuned. This nearly model-free controller is expected to display higher motion control performances than conventional controllers such as the computed torque control methods.

The stability and performance analysis of PD control applied to PMs is addressed in ref. [35]. It is important to note that the task-space controller is not implemented as a stand-alone controller in this study. Instead, the task-space controller will be employed as an auxiliary control method to correct the shortcomings of the joint-space controller, thereby ensuring robust performance and stability of the overall system. In the hybrid joint-space control method proposed in Section 3.1, a reaching law and a DOB have been introduced. The combined joint and task-space controller is designed to further enhance controller performance and prevent singularity in PMs. In PMs, the joint-space controller relies upon the leg lengths measured by encoders to determine the end-effector's position and orientation. However, in certain configurations, the leg lengths may be identical for both positive and negative end-effector positions, leading to ambiguous solutions due to singularities. This presents challenges for the controller in accurately determining joint angles to achieve desired end-effector positions and orientations. The combined controller is based on both joint space and task space, namely, joint and end-effector position. Hence, by integrating both joint and task-space control strategies, the overall system can achieve improved performance and robustness across various operating conditions.

3.2.1. Stability analysis of combined control method

Let us consider the following Lyapunov function candidate V_2 and its time derivative:

$$V_2 = \frac{1}{2} \mathbf{s}(t)^T \mathbf{s}(t) + \frac{1}{2} \mathbf{e}_{\text{dis}}^T \mathbf{e}_{\text{dis}} \tag{55}$$

$$\dot{V}_2 = \mathbf{s}\dot{\mathbf{s}} + \mathbf{e}_{\text{dis}}\dot{\mathbf{e}}_{\text{dis}} \tag{56}$$

Substituting the combined control law inside the dynamic model in joint space, one gets the following closed-loop acceleration dynamic model:

$$\begin{aligned} \ddot{\mathbf{q}}(t) = & \ddot{\mathbf{q}}_r(t) + k_0 \operatorname{sgn}(\mathbf{s}(t)) + \eta \mathbf{s}(t) + \lambda \dot{\mathbf{e}}(t) \\ & + M_n(\mathbf{q})^{-1} [\boldsymbol{\tau}_{\text{dob}}(t, \mathbf{q}) - \boldsymbol{\tau}_{\text{dis}}(t, \mathbf{q})] \\ & + M_n(\mathbf{q})^{-1} J^T \mathbf{r}(t) \end{aligned} \tag{57}$$

The time derivative of the sliding surface is given as follows:

$$\dot{\mathbf{s}}(t) = \ddot{\mathbf{q}}_r(t) - \ddot{\mathbf{q}}(t) + \lambda(\dot{\mathbf{q}}_r(t) - \dot{\mathbf{q}}(t)) \tag{58}$$

Substituting Eq. (57) into (58) yields as follows:

$$\dot{\mathbf{s}}(t) = -k_0 \operatorname{sgn}(\mathbf{s}(t)) - \eta \mathbf{s}(t) - M_n(\mathbf{q})^{-1} \mathbf{e}_{\text{dis}}(t) - M_n(\mathbf{q})^{-1} J^T \mathbf{r}(t) \tag{59}$$

Now inserting Eq. (59) into Eq. (56) results in the following expression of \dot{V}_2 :

$$\dot{V}_2 = \mathbf{s}(t)(-k_0 \operatorname{sgn} \mathbf{s}(t) - \eta \mathbf{s}(t) - M_n^{-1} \mathbf{e}_{\text{dis}} - M_n(\mathbf{q})^{-1} J^T \mathbf{r}(t)) - LM_n^{-1} \|\mathbf{e}_{\text{dis}}\|^2 \tag{60}$$

Considering $\|\mathbf{e}_{\text{dis}}(0)\| = \|\mathbf{e}_{\text{dis}}\|_{\text{max}}$, and $k_0 \geq M_n^{-1} \|\mathbf{e}_{\text{dis}}(0)\|$, then

$$\dot{V}_2 \leq -\eta \|\mathbf{s}(t)\|^2 - LM_n^{-1} \|\mathbf{e}_{\text{dis}}\|^2 - \mathbf{s}(t) M_n(\mathbf{q})^{-1} J^T \mathbf{r}(t) \tag{61}$$

With $k = 1$ and $\lambda = c$, the sliding mode in joint-space $\mathbf{s}(t)$ and sliding mode in task-space $\mathbf{r}(t)$ have the following relationship:

$$\mathbf{s}(t) = J^T \mathbf{r}(t) \tag{62}$$

Hence, the last terms in \dot{V}_2 equation can be written as follows:

$$-\mathbf{s}(t) M_n(\mathbf{q})^{-1} J^T \mathbf{r}(t) = -\mathbf{s}(t) M_n(\mathbf{q})^{-1} \mathbf{s}(t) \tag{63}$$

This expression now represents a quadratic form involving the vector $\mathbf{s}(t)$ and the inverse of the inertia matrix $M_n(\mathbf{q})^{-1}$. When the intention is to interpret the result as a weighted norm, we typically write

$$-\mathbf{s}(t)^T M_n(\mathbf{q})^{-1} \mathbf{s}(t) = -M_n(\mathbf{q})^{-1} \|\mathbf{s}(t)\|^2 \tag{64}$$

Hence, inserting Eq. (64) into Eq. (60) yields the following:

$$\dot{V}_2 \leq -\eta \|\mathbf{s}(t)\|^2 - LM_n^{-1} \|\mathbf{e}_{\text{dis}}\|^2 - M_n(\mathbf{q})^{-1} \|\mathbf{s}(t)\|^2 \tag{65}$$

Factoring out for the same terms:

$$\dot{V}_2 \leq -(\eta + M_n^{-1}) \|\mathbf{s}(t)\|^2 - LM_n^{-1} \|\mathbf{e}_{\text{dis}}\|^2 \tag{66}$$

$$\dot{V}_2 \leq -k_3 \left(\frac{1}{2} \mathbf{s}(t)^T \mathbf{s}(t) + \frac{1}{2} \mathbf{e}_{\text{dis}}^T \mathbf{e}_{\text{dis}} \right) \tag{67}$$

$$\dot{V}_2 \leq -k_3 V_2 \tag{68}$$

where $k_3 = 2 \min\{(\eta + M_n^{-1}), LM_n^{-1}\}$.

Based on the same Lemma [37] again, one gets

$$V_2(t) \leq e^{-k_3(t-t_0)} V_2(t_0) \tag{69}$$

If k_3 has a positive constant value, then $V_2(t)$ will tend to zero exponentially. Specifically, the right side of inequality decreases linearly as time t increases, and so the function will converge to zero exponentially, showing the stability of the proposed controller.

4. Simulations

To validate proposed control techniques both simulations and experimental tests are conducted. A comprehensive dynamic model of the experimental platform is built in MATLAB/Simulink R2023b environment for a numerical evaluation of the performances of the proposed controllers' techniques. The dynamic model is built in Simscape Simulink environment. Inverse kinematics, forward kinematics, and Jacobian matrix are coded as MATLAB functions. As detailed in the next section, for the experimental validation of the proposed controller, disturbances corresponding to Level-4 and Level-5 sea states are used as reference signals. Similarly, these sea state disturbances are employed as input signals in the simulation model. To ensure fair comparisons between simulations and real-time experiments, fundamental parameters such as sampling frequency, controller gains, and input signals are kept identical.

Figure 3 depicts the position tracking errors of all six axes of the platform simulated under the Level-4 sea state conditions. Table I details the RMS position tracking errors for the 6-DoF of the moving platform, comparing the performances of the considered controllers. Figure 4 depicts the position tracking errors of all six axes of the platform simulated under the Level-5 sea state conditions. Table II details the RMS position tracking errors for the 6-DoF of the moving platform, comparing the performances of the considered controllers. Simulation results show that the hybrid controller nearly halved the positional errors, while the combined controller reduced them to about four times compared to the ACC method. Furthermore, the control efforts or leg forces, represented as currents, are of a similar order of magnitude in amplitude. As a result, position tracking precision is improved without requiring additional servomotor power.

Tables III and IV list the RMS control efforts or control forces in terms of motor currents for x , y , z , roll, pitch, and yaw axes for the Level-4 sea state and Level-5 sea state conditions, respectively. Comparing the simulation results with the experimental results in terms of position tracking errors and control efforts, one can observe a certain consistency between these two analysis approaches. Hence, the performance of the proposed controller methods is verified numerically through detailed modeling and simulations, consistent with real-time experimental results as shown in the next section.

5. Experimentations

The proposed controllers are implemented on a 6-DoF Stewart platform test setup shown in Figure 2. Geometric specification of the test setup is given in Table V. The main components of the platform include universal joints, reducers, servomotors, ball screws, and upper and lower frames. Drivers, power supplies, filters, safety components, and other I/O modules are enclosed in an electrical cabinet. The sensory system consists of inertial measurement units (IMUs), encoders, and limit switches. For joint-space control, the leg lengths are measured by high-resolution encoders integrated into the servomotors. For task-space control, IMUs are located at the center of the upper frame. One IMU is used for control purposes and another for measuring the performance of the proposed controllers. The control algorithm is programmed in C/C++ and implemented on a real-time industrial PC with high sampling frequency. Each of the six legs is controlled separately as a single DoF. The legs are composed of identical servomotors, reducers, joints, bearings, and ball screws. Additionally, the control algorithm and other software are the same for all six legs. So the legs are identical in terms of all hardware and software.

The payload on the 6-DoF test setup is used on a marine vehicle for stabilization purposes of camera or antenna mostly in the Level-4 and Level-5 sea state conditions. In order to establish a test environment in a laboratory for the payload, the 6-DoF test setup needs to replicate the marine conditions characterized by wave heights and periods. This involves generating time-series data representing the 6-DoF: heave,

Table I. Simulation: RMS tracking errors for Level-4 sea state input signals.

Control methods	X (mm)	Y (mm)	Z (mm)	Roll (°)	Pitch (°)	Yaw (°)
ACC	0.42	0.43	0.54	0.04	0.04	0.02
Hybrid	0.25	0.27	0.35	0.02	0.02	0.01
Combined	0.13	0.12	0.17	0.01	0.01	0.01

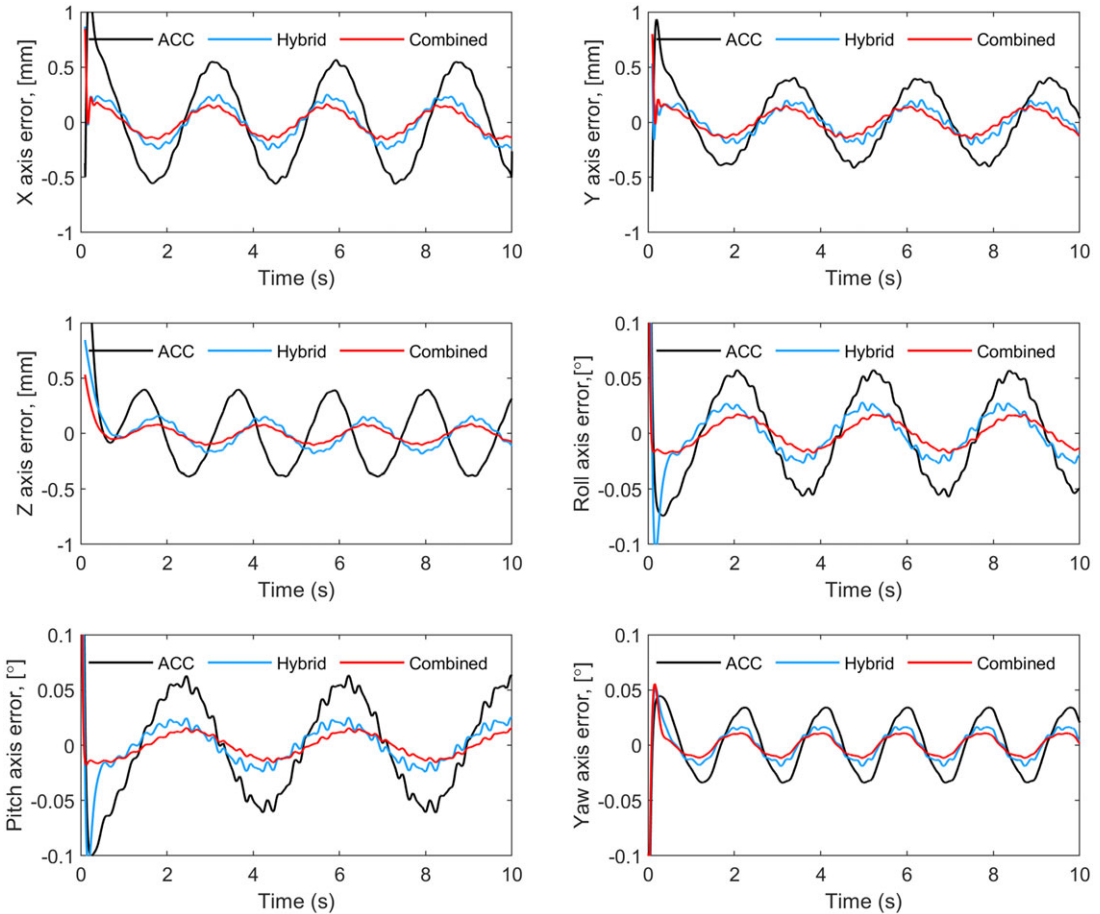


Figure 3. Simulation: end-effector position tracking errors in Level-4 sea state conditions.

pitch, roll, surge, sway, and yaw. The generated data should then be scaled appropriately to match Level-4 and Level-5 sea state conditions in workspace limits of the test setup. This setup allows for rigorous testing of the stabilization performance under marine conditions. The aim of the 6-DoF test setup as a controlled system is to track these signals accurately.

In this study, disturbances corresponding to Level-4 and Level-5 sea states are considered as input signals. These inputs represent external disturbances applied to marine vehicles during operations. The Level-4 and Level-5 sea state signals' amplitudes and frequencies that range from 0.25 Hz to 0.73 Hz and 10° to 15° are taken from the marine standard document of Interface Standard for Shipboard Systems given in ref. [38]. The payload mass is 50 kg, and the mass moment of inertias are 20, 21, and 18 kg.m² around X, Y, and Z axis, respectively. For real-time experiments, the controller parameters are set as

Table II. Simulation: RMS tracking errors for Level-5 sea state input signals.

Control methods	X (mm)	Y (mm)	Z (mm)	Roll (°)	Pitch (°)	Yaw (°)
ACC	0.51	0.53	0.61	0.05	0.05	0.03
Hybrid	0.33	0.34	0.41	0.03	0.03	0.01
Combined	0.19	0.18	0.25	0.01	0.01	0.01

Table III. Simulation: RMS currents (in Amp) for Level-4 sea state input signals.

Control methods	X	Y	Z	Roll	Pitch	Yaw
ACC	7.5	7.6	9.5	5.1	7.3	6.6
Hybrid	7.6	7.7	9.9	5.6	7.5	6.5
Combined	7.6	8.9	9.7	5.7	7.7	6.5

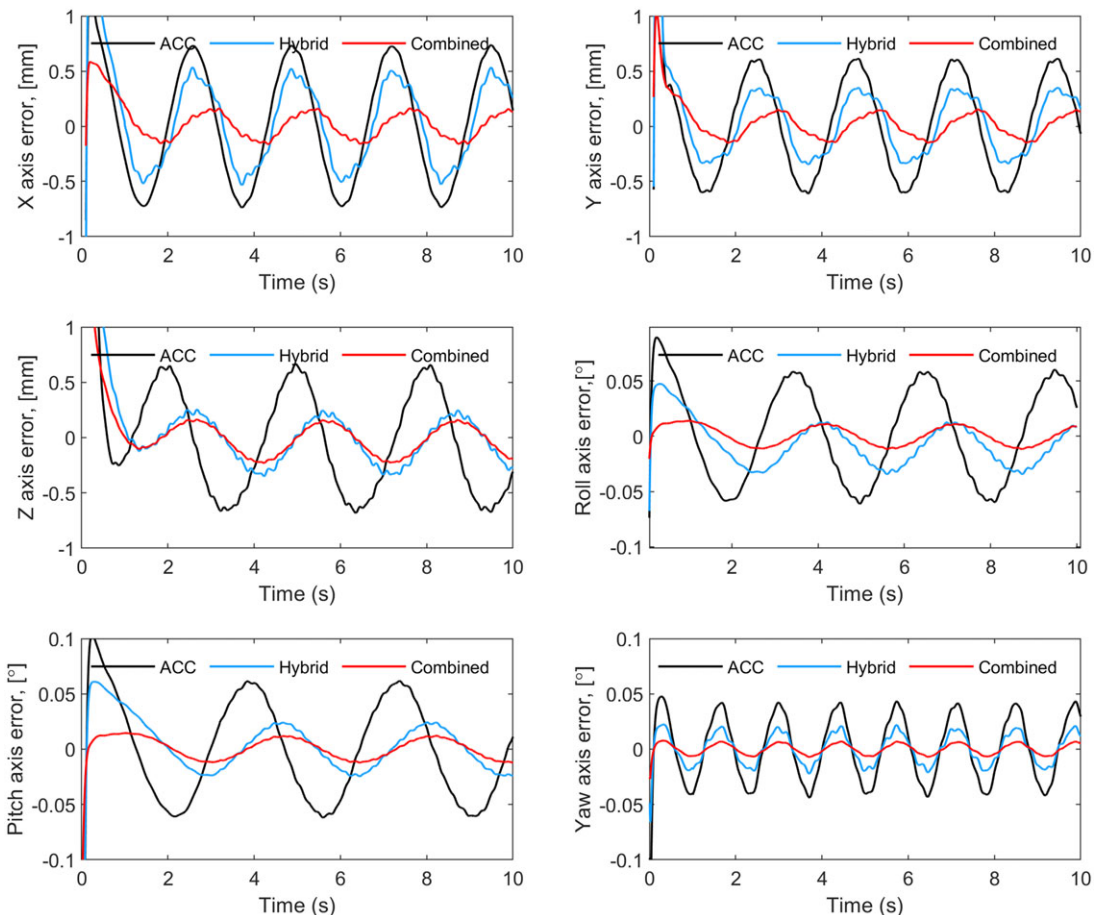


Figure 4. Simulation: end-effector position tracking errors in Level-5 sea state conditions.

$k_p = 80, k_v = 10, k_0 = 20, \lambda = 2, c = 5, k = 2$. Also, the bandwidth of DOB is $L = 300$ Hz, and the nominal inertia projected to the motor side is $M_n = 0.1$.

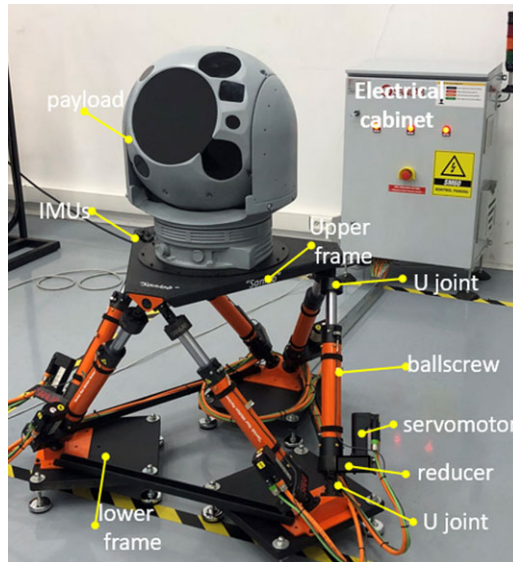
To evaluate the performance of the Stewart platform, it is focused on the position tracking error of the end-effector or moving platform by measuring deviations from the input signals. This involves

Table IV. Simulation: RMS currents (in Amp) for Level-5 sea state input signals.

Control methods	X	Y	Z	Roll	Pitch	Yaw
ACC	8.4	8.5	10.5	5.9	8.2	7.1
Hybrid	8.5	8.6	10.7	6.1	8.3	7.4
Combined	8.8	9.8	10.9	6.3	8.6	7.6

Table V. Geometric specification of the test setup.

Parameters	Base radius	Moving radius	Settled height	Neutral height	Stroke
Values [mm]	340	450	470	580	220

**Figure 5.** 6-DoF parallel manipulator for real-time experimental studies.

comparing the actual positions and orientations of the platform with the desired trajectories generated for the 6-DoF: heave, pitch, roll, surge, sway, and yaw. Additionally, control efforts, which include the forces and torques exerted by the actuators, are recorded. These efforts are compared across different control methods to determine which method provides the best performance in terms of minimizing tracking errors and optimizing control efforts. Figure 6 and Figure 7 illustrate the position errors for the x, y, z, roll, pitch, and yaw axes under the Level-4 and Level-5 sea state condition signals, respectively. The performance of acceleration-based (ACC), hybrid joint-space (Hybrid), and combined joint and task-space control (combined) methods are evaluated for all axes. Tables VI and VII present the position tracking error root mean square error for all axes across different control methods. Experimental results indicate that the position errors are reduced by nearly 50% with the proposed hybrid controller compared to the ACC method. Furthermore, when using the proposed combined controller, the position errors are reduced by nearly threefold compared to the ACC method.

Figures 8 and 9 illustrate the control efforts in terms of currents measured for the first leg of the Stewart platform subjected to Level-4 and Level-5 sea state disturbance signals. Although all six legs are in motion for each axis test, for clarity and brevity, only the current for one motor in the first leg is presented here. However, analogous behavior is observed for the motor currents in the remaining legs. One can observe from Figures 8 and 9 that the ACC controller exhibits noticeable oscillations in

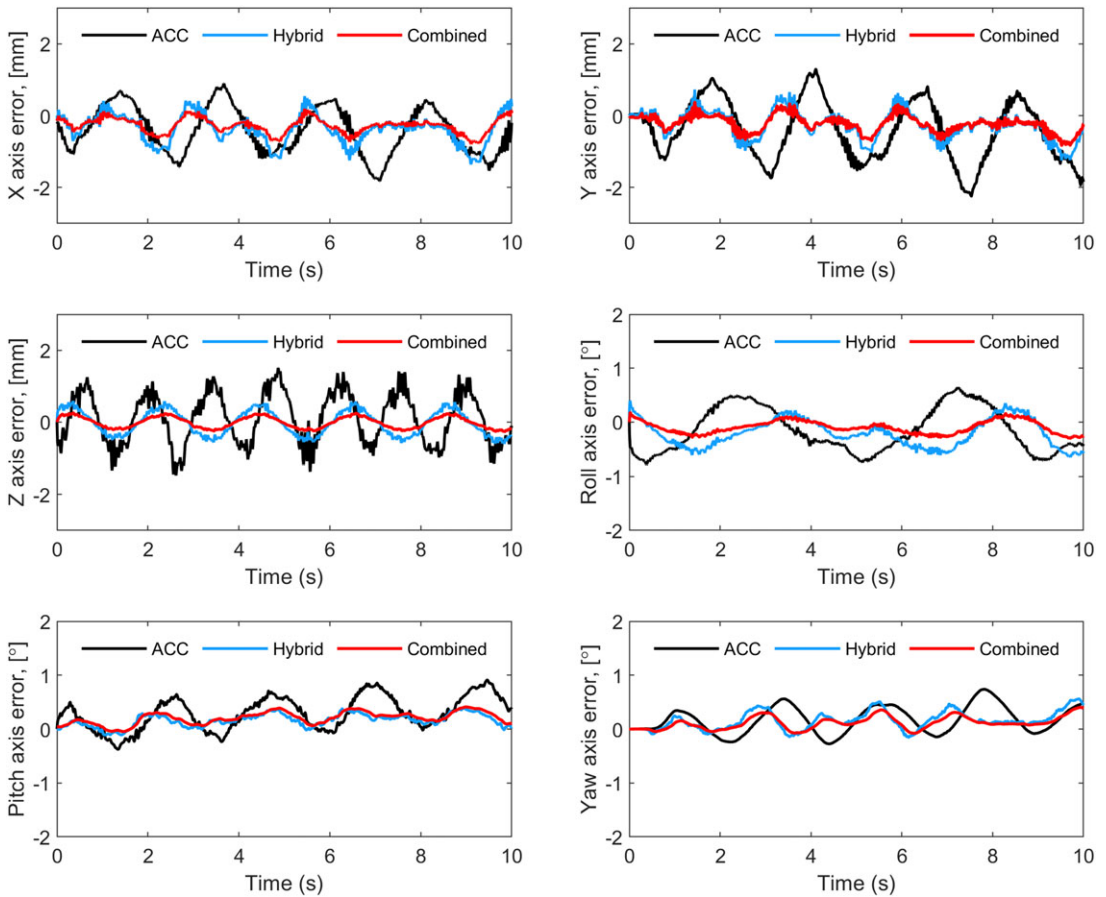


Figure 6. End-effector position errors for X-Y-Z positional and roll-pitch-yaw rotational axes under Level-4 sea state input signals.

control efforts, characterized by significant fluctuations in motor currents. These oscillations indicate instability and can potentially affect the performance of the Stewart platform, as depicted in Figure 6 and Figure 7. However, the proposed hybrid and combined controllers methods effectively mitigate these oscillations and overshoots. Comparative analysis highlights improvements with hybrid and combined controllers compared to the ACC approach, resulting in smoother responses and reduced current oscillations.

Tables VIII and IX show the root mean square control efforts or leg forces in terms of measured currents of the motor in the first leg under Level-4 and Level-5 sea states, respectively. Although all six legs are in motion for each axis test, for clarity and brevity, only the current for one motor in the first leg is presented here. However, analogous behavior is observed for the motor currents in the remaining legs. This comparison shows that the control efforts are similar order of magnitude in terms of amplitude. Hence, the position tracking precision is enhanced without consuming additional servomotor power.

The results indicate similar performances across both sea states in terms of position tracking errors and control efforts measured in terms of the motor currents drawn. This consistency suggests that the control strategies evaluated are robust across different sea state intensities, demonstrating stable performance in maintaining accurate positioning and effective control of the Stewart platform under varying input signals experimentation.

Table VI. RMS tracking errors for X-Y-Z-roll-pitch-yaw axes under Level-4 sea state input signals.

Control methods	X (mm)	Y (mm)	Z (mm)	Roll (°)	Pitch (°)	Yaw (°)
ACC	0.81	0.87	0.75	0.43	0.47	0.25
Hybrid	0.53	0.45	0.37	0.17	0.24	0.11
Combined	0.37	0.33	0.21	0.11	0.14	0.07

Table VII. RMS position tracking errors for X-Y-Z-roll-pitch-yaw axes under Level-5 sea state input signals.

Control methods	X (mm)	Y (mm)	Z (mm)	Roll (°)	Pitch (°)	Yaw (°)
ACC	0.88	0.98	0.89	0.53	0.47	0.31
Hybrid	0.63	0.55	0.41	0.25	0.24	0.15
Combined	0.45	0.39	0.25	0.13	0.14	0.07

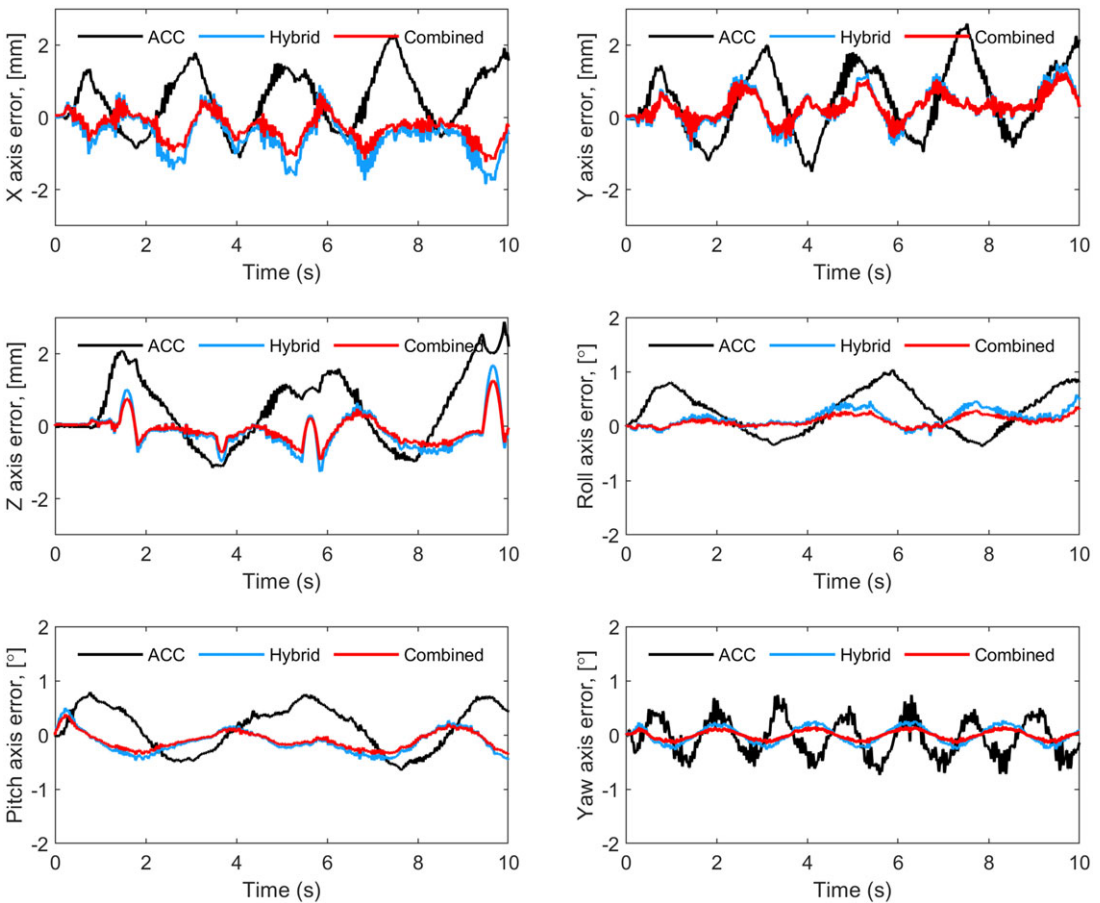


Figure 7. End-effector position errors for X-Y-Z positional and roll-pitch-yaw rotational axes under Level-5 sea state input signals.

Table VIII. RMS currents (in Amp) for X-Y-Z-roll-pitch-yaw axes under Level-4 sea state input signals.

Control methods	X	Y	Z	Roll	Pitch	Yaw
Acc	9.4	7.4	13.1	6.9	9.1	7.6
Hybrid	9.7	7.8	13.5	7.1	9.4	7.7
Combined	10.0	8.1	13.8	7.4	9.7	7.8

Table IX. RMS currents (in Amp) for X-Y-Z-roll-pitch-yaw axes under Level-5 sea state input signals.

Control methods	X	Y	Z	Roll	Pitch	Yaw
ACC	10.6	8.9	13.9	7.9	9.5	8.3
Hybrid	10.7	9.0	14.4	8.2	9.8	8.4
Combined	10.9	9.3	14.6	8.5	10.1	8.5

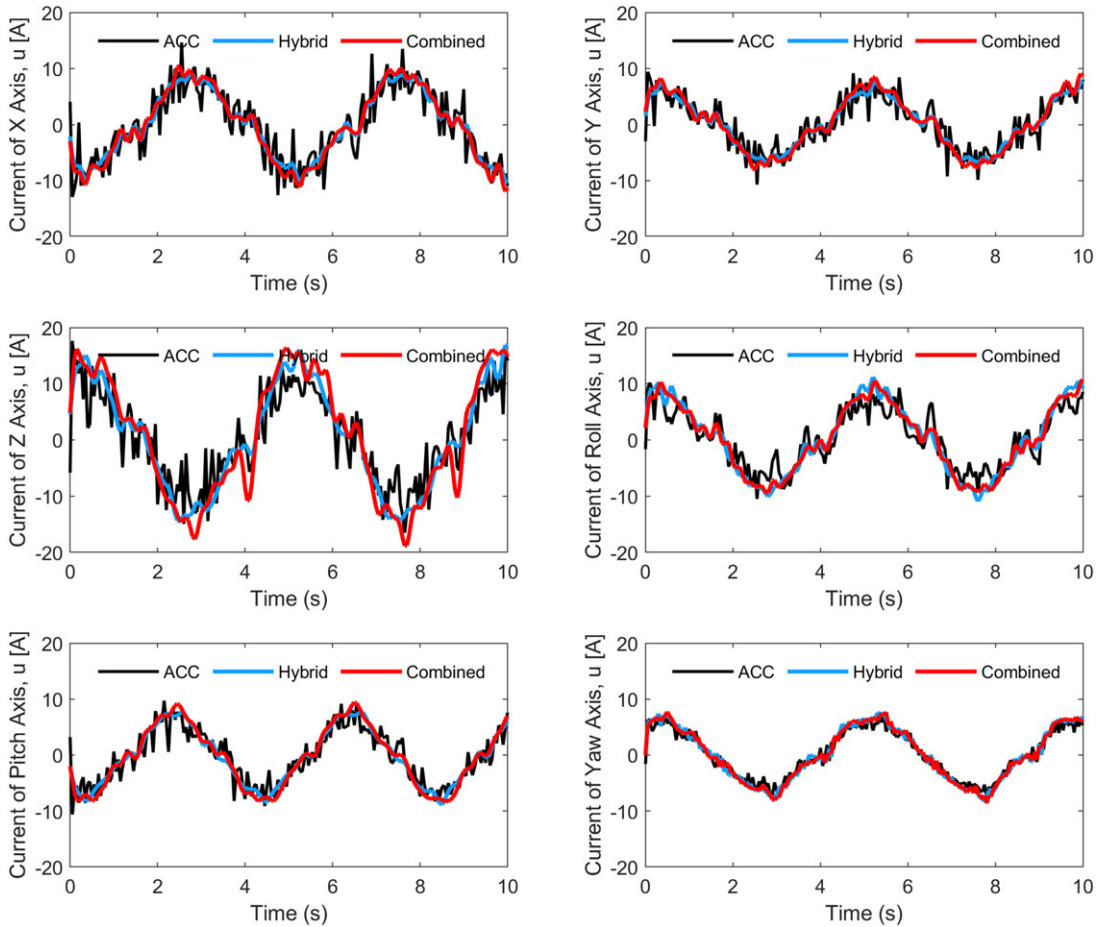


Figure 8. Motor currents values of the first leg for X-Y-Z positional and roll-pitch-yaw rotational axes under Level-4 sea state input signals.

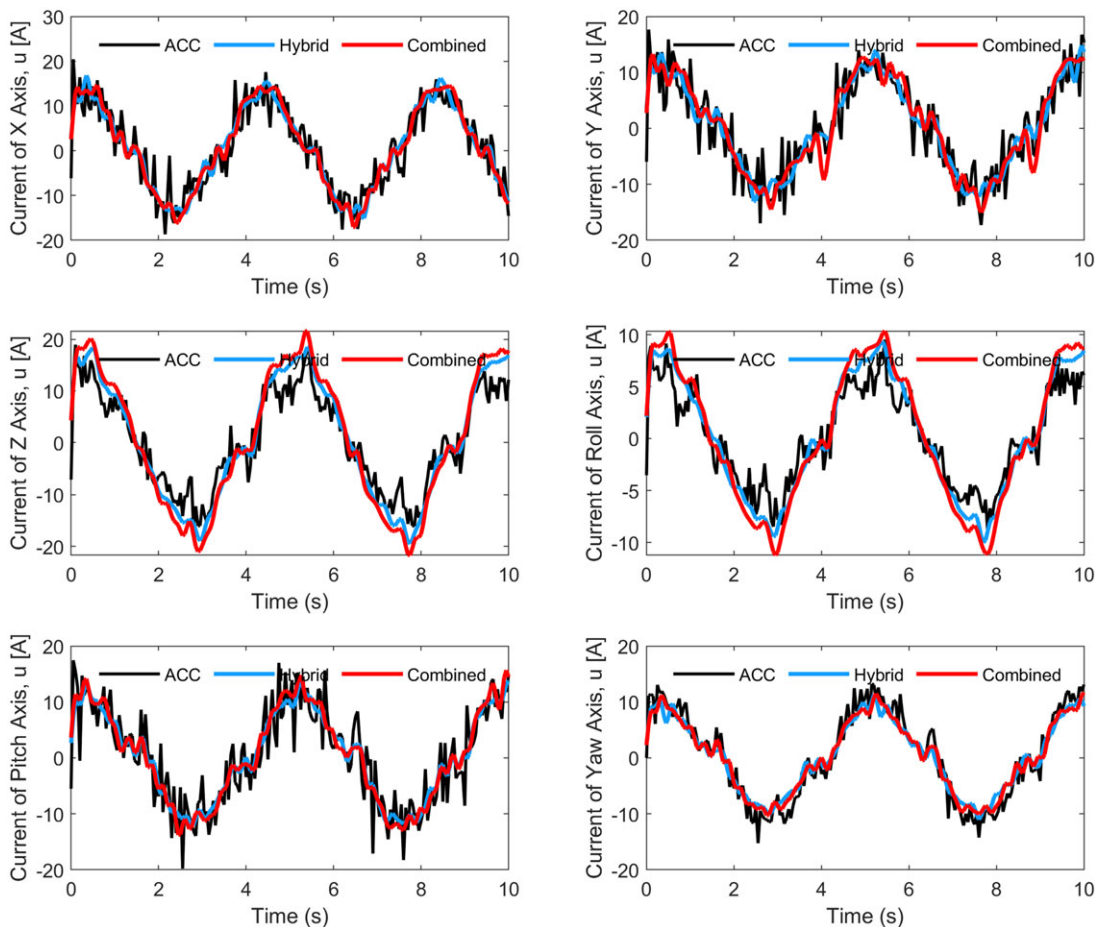


Figure 9. Motor currents values of the first leg for X-Y-Z positional and roll-pitch-yaw rotational axes under Level-5 sea state input signals.

Figures 10 and 11 further illustrate the frequency spectra of the motor current signals observed in Figure 8 and Figure 9. The introduction of the proposed controllers results in a notable reduction of high-frequency components within the current signals compared to the acceleration-based approach. This enhancement in motor current signal quality plays a critical role in maintaining reliable stabilization of the 6-DoF Stewart platform, thereby improving overall performance and operational effectiveness.

6. Conclusion

This study presents two innovative control strategies that significantly enhance the performance of PMs by addressing their intrinsic nonlinear dynamics and complex structures. The first strategy employs a hybrid control system in joint space, combining AbC, sliding mode, and DOB techniques. This integrated approach effectively corrects errors and compensates for generalized disturbances, leading to improved accuracy in tracking reference positions without the need for an additional sensor. Experimental and simulation results show that this method significantly enhances performance, eliminates current oscillations, and achieves more stable and precise positioning although the control efforts remain comparable in magnitude.

The second strategy integrates the joint-space and task-space controls, using PD-like sliding surface control in task space to precisely manage the end-effector positions while ensuring safe operational configurations. This combined control method produces the best results, achieving high positioning

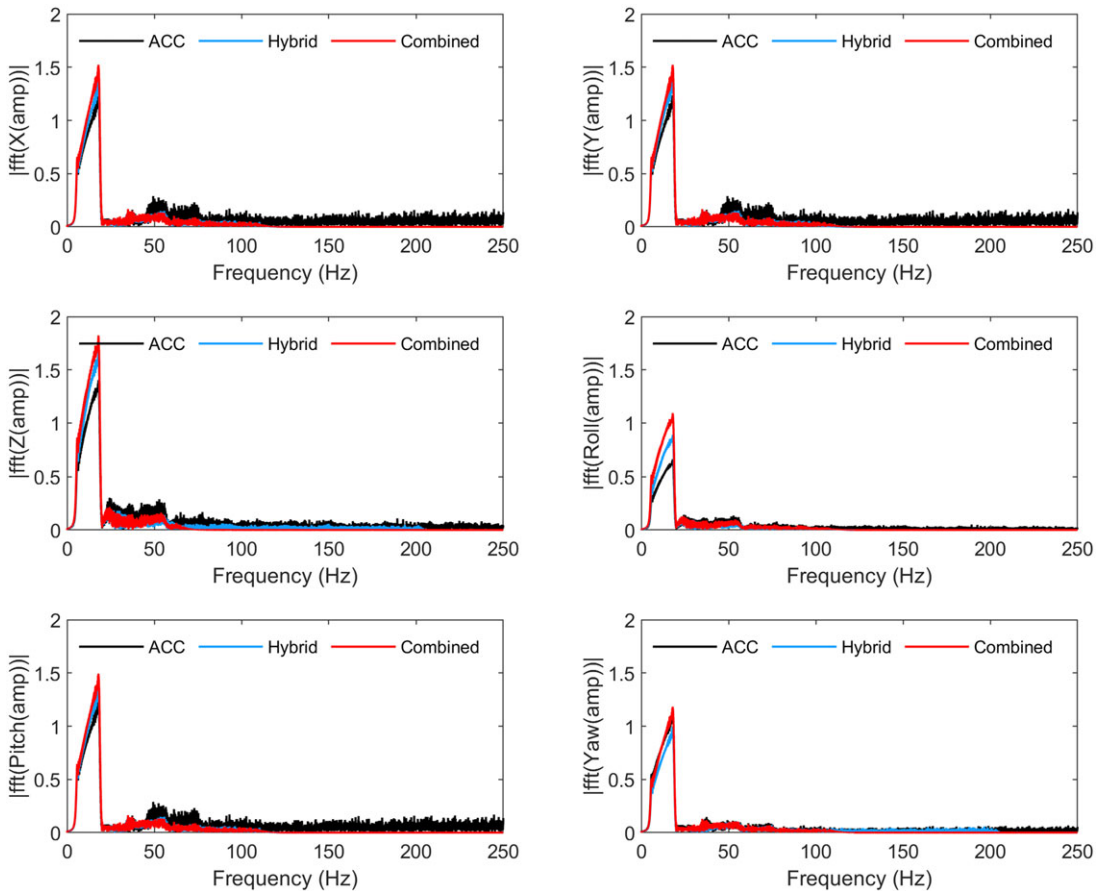


Figure 10. Frequency spectra (through FFT) of the motor currents values of the first leg for X-Y-Z-roll-pitch-yaw axes under Level-4 sea state input signals.

accuracy and increased system stability. Furthermore, the combined joint and task-space controller prevents singularities in PMs. In these manipulators, the joint-space controller uses leg lengths, measured by encoders, to determine the end-effector position and orientation. However, identical leg lengths in certain configurations can cause ambiguity, leading to singularities and making it challenging to accurately determine the joint positions. By integrating the joint-space and task-space control strategies, the combined controller improves overall system performance and robustness.

The efficiency of these proposed control methodologies is validated through the Lyapunov stability analysis, extensive simulations, and real-time experiments. In the experiments, the sea state conditions of Level-4 and Level-5 data (from the Interface Standard for Shipboard Systems) are used to test the performances of the proposed controllers. The results show that both control strategies offer substantial improvements in motion tracking precision and stability of PMs. By enhancing the manipulators' ability to accurately track the reference trajectories and maintain stability under various operational conditions, these proposed control techniques represent a significant contribution in the field of robotic control systems. Future research may further refine these strategies and explore their applications in more complex and dynamic environments, potentially broadening their scope and impact in industrial and research settings.

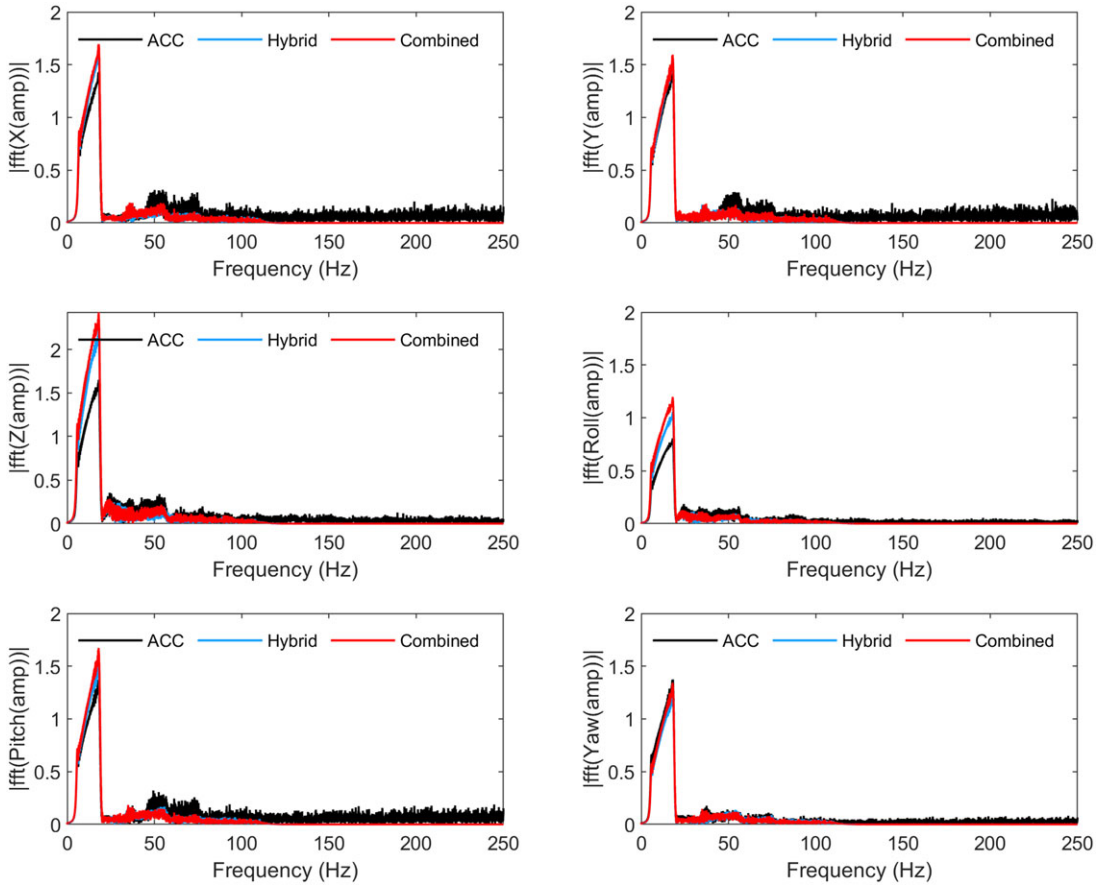


Figure 11. Frequency spectra (through FFT) of the motor currents values of the first leg for X-Y-Z-roll-pitch-yaw axes under Level-5 sea state input signals.

Author contributions. ES conducted the study and wrote the article, while ZYB provided comprehensive supervision throughout all stages of the project, including reviewing and editing the article.

Financial support. This research received no specific grant from any funding agency, commercial, or not-for-profit sectors.

Competing interests. The authors declare no conflicts of interest exist.

Ethical approval. Not applicable.

References

- [1] D. Stewart, "A platform with six degrees of freedom," *Proc. Inst. Mech. Eng.* **180**(1), 371–386 (1965).
- [2] A. Bertelsen, J. Melo, E. Sánchez and D. Borro, "A review of surgical robots for spinal interventions," *Int. J. Med. Robot.* **9**(4), 407–422 (2013).
- [3] Y. Cai, S. Zheng, W. Liu, Z. Qu and J. Han, "Model analysis and modified control method of ship-mounted Stewart platforms for wave compensation," *IEEE Access* **9**, 4505–4517 (2021).
- [4] H. Ren, L. Zhang and C. Su, "Design and research of a walking robot with two parallel mechanisms," *Robotica* **39**(9), 1634–1641 (2021).
- [5] K. Herbuś and P. Ociełka. Integration of the Virtual Model of a Stewart Platform with the Avatar of a Vehicle in a Virtual Reality. In: *IV International Conference on Modern Technologies in Industrial Engineering (Iasi, Romania, 15-18 June 2016)* (2016) pp. 519–524.

- [6] A. Müller, "Problems in the control of redundantly actuated parallel manipulators caused by geometric imperfections," *Meccanica* **46**(1), 41–49 (2011).
- [7] G. S. Natal, A. Chemori and F. Pierrot, "Nonlinear control of parallel manipulators for very high accelerations without velocity measurement: Stability analysis and experiments on Par2 parallel manipulator," *Robotica* **34**(1), 43–70 (2016).
- [8] K. V. Sancak and Z. Y. Bayraktaroglu, "Observer-based friction compensation in heavy-duty parallel robot control," *J. Mech. Sci. Technol.* **35**(8), 3693–3704 (2021).
- [9] J. P. Merlet. *Parallel Robots*. 2nd edition (Springer, Dordrecht, Netherlands, 2006).
- [10] M. W. Spong, S. Hutchinson and M. Vidyasagar. *Robot Modeling and Control* (Wiley, Hoboken, NJ, USA, 2005).
- [11] E. V. L. Nunes and L. Hsu, "Global tracking for robot manipulators using a simple PD controller plus feedforward," *Robotica* **28**(1), 23–34 (2010).
- [12] A. A. Pervozvanski and L. B. Freidovich, "Robust stabilization of robotic manipulators by PID controllers," *Dyn. Control* **9**(3), 203–222 (1999).
- [13] J. J. Craig. *Introduction to Robotics: Mechanics and Control* (Prentice Hall, Englewood Cliffs, NJ, USA, 2004).
- [14] I. Cervantes and J. Alvarez-Ramirez, "On the PID tracking control of robot manipulators," *Syst. Control Lett.* **42**(1), 37–46 (2001).
- [15] M. Bennehar, Some Contributions to Nonlinear Adaptive Control of PKMs: From Design to Real-Time Experiments (PhD thesis) (Université Montpellier, Automatics, 2015).
- [16] M. U. Daniş and Z. Y. Bayraktaroglu. "Implementation of an Adaptive Control Algorithm on a Six-DOF Robot Manipulator." **In: Proc. 9th Int. Conf. Control, Decision and Inf. Technol.** (2023) pp. 2170–2175.
- [17] M. R. J. Harandi, S. A. Khalilpour, H. D. Taghirad and J. G. Romero, "Adaptive control of parallel robots with uncertain kinematics and dynamics," *Mech. Syst. Signal Process.* **157**, 107676 (2021).
- [18] V. I. Utkin, J. Guldner and J. Shi, *Sliding Mode Control in Electro-Mechanical Systems* (2nd edition, CRC Press, Boca Raton, FL, USA, 2017).
- [19] M. Zeinali and L. Notash, "Adaptive sliding mode control with uncertainty estimator for robot manipulators," *Mech. Mach. Theory* **45**(1), 80–90 (2010).
- [20] J.-J. E. Slotine and W. Li. *Applied Nonlinear Control* (Prentice Hall, Englewood Cliffs, NJ, USA, 1991).
- [21] A. Dumlu and K. Erenturk, "Modeling and trajectory tracking control of 6-DOF RSS type parallel manipulator," *Robotica* **32**(4), 643–657 (2014).
- [22] H. Yadavari, V. T. Aghaei and S. İkiçoğlu, "Deep reinforcement learning-based control of Stewart platform with parametric simulation in ROS and Gazebo," *J. Mech. Robot.* **15**(3), 061005 (2023).
- [23] A. Naderolasli, K. Shojaei and A. Chatraei, "Terminal sliding-mode disturbance observer-based finite-time adaptive-neural formation control of autonomous surface vessels under output constraints," *Robotica* **41**(1), 236–258 (2023).
- [24] V. E. Ömürlü and I. Yildiz, "Self-tuning fuzzy PD-based stiffness controller of a 3 × 3 Stewart platform as a man-machine interface," *Turk. J. Electr. Eng. Comput. Sci.* **19**(5), 743–752 (2011).
- [25] X. Li and G. Gao, "An intelligent fixed-time super-twisting sliding mode control of the uncertain hybrid mechanism," *Robotica* **42**, 1–20 (2024).
- [26] G. S. Natal, A. Chemori and F. Pierrot, "Dual-space control of extremely fast parallel manipulators: Payload changes and the 100G experiment," *IEEE Trans. Control Syst. Technol.* **23**(4), 1520–1535 (2015).
- [27] A. Castañeda, A. Luviano-Juárez and I. Chairez, "Robust trajectory tracking of a delta robot through adaptive active disturbance rejection control," *IEEE Trans. Control Syst. Technol.* **23**(4), 1387–1398 (2015).
- [28] A. Chemori, R. Kouki and F. Bouani, "A new fast nonlinear model predictive control of parallel manipulators: Design and experiments," *Control Eng. Pract.* **130**, 105186 (2023).
- [29] M. Rachedi and H. Bouri, "Design of an H_∞ controller for the delta robot: Experimental results," *Adv. Robot.* **29**(18), 1165–1181 (2015).
- [30] A. G. Coutinho and T. A. Hess-Coelho, "Improving the performance of parallel robots by applying distinct hybrid control techniques," *Robotica* **40**(4), 951–975 (2021).
- [31] J. V. de C. Fontes, F. T. Colombo, N. B. F. da Silva and M. M. da Silva, "Model-based joint and task space control strategies for a kinematically redundant parallel manipulator," *Robotica* **40**(5), 1570–1586 (2022).
- [32] T. Kara and A. L. Mary, "Adaptive PD-SMC for nonlinear robotic manipulator," *Track. Control Stud. Inf. Control* **26**(1), 49–58 (2017).
- [33] D. Shiferaw and A. Jain. "Comparison of Joint-Space and Task Space Integral Sliding Mode Controller Implementations of a 6-DOF Parallel Robot." **In: Proc. 11th WSEAS Int. Conf. Robot. Control Manuf. Technol.** (2011).
- [34] P. R. Kumar, A. Chalanga and B. Bandyopadhyay, "Smooth integral sliding mode controller for the position control of Stewart platform," *ISA Trans.* **58**, 543–551 (2015).
- [35] Z. H. Qu, "Global stability of trajectory tracking of robot under PD control," *Dyn. Control* **5**(1), 59–71 (1995).
- [36] J. Liu. *Sliding Mode Control Using MATLAB* (A. Press, 2017).
- [37] P. A. Ioannou and J. Sun, *Robust Adaptive Control* (PTR Prentice-Hall, Upper Saddle River, NJ, USA (1996).
- [38] DOD-STD-1399/301A. *Department of Defense Interface Standard: Interface Standard for Shipboard Systems Section 301A Ship Motion and Attitude* (U.S. Department of Defense, Washington, DC, USA).
- [39] A. N. Atassi and H. K. Khalil, "A separation principle for the stabilization of a class of nonlinear systems," *IEEE Trans. Autom. Control* **44**(9), 1672–1687 (1999). doi: [10.1109/9.788534](https://doi.org/10.1109/9.788534).
- [40] E. Sariyildiz, R. Oboe and K. Ohnishi, "Disturbance observer-based robust control and its applications: 35th anniversary overview," *IEEE Trans. Ind. Electron.* **67**(3), 2042–2053 (2020).

- [41] C. O. Saglam, E. A. Baran, A. O. Nergiz and A. Sabanovic. "Model following control with discrete-time SMC for time-delayed bilateral control systems," *Proc. IEEE Int. Conf. Mechatron.*, 997–1002. (2011).
- [42] A. Mohammadi, M. Tavakoli, H. J. Marquez and F. Hashemzadeh, "Nonlinear disturbance observer design for robotic manipulators, control engineering practice," *Control Eng. Pract.* 253–267 (2013).